The Astrophysical Journal, 935:32 (13pp), 2022 August 10 https://doi.org/10.3847/1538-4357/ac73f5

Dependence of Energetic Storm Particle Heavy Ion Peak Intensities and Spectra on Source CME Longitude and Speed

A. Santa Fe Dueñas[1,2], R. W. Ebert[1,2], M. A. Dayeh[1,2], M. I. Desai[1,2], L. K. Jian[3], G. Li[4], and C. W. Smith[5]
[1] Department of Physics and Astronomy, University of Texas at San Antonio, San Antonio, TX 78249, USA; adolfo.santafeduenas@my.utsa.edu
[2] Space Science and Engineering Division, Southwest Research Institute, San Antonio, TX 78228, USA
[3] NASA Goddard Space Flight Center, USA
[4] University of Alabama in Huntsville, USA
[5] University of New Hampshire, USA
Received 2021 December 30; revised 2022 May 11; accepted 2022 May 25; published 2022 August 10

Abstract

We examine variations in energetic storm particle (ESP) heavy ion peak intensities and energy spectra at CME-driven interplanetary shocks. We focus on their dependence with heliolongitude relative to the source region of their associated CMEs, and with CME speed, for events observed in Solar Cycle 24 at the STEREO-A, STEREO-B, and/or ACE spacecraft. We find that observations of ESP events at 1 au are organized by longitude relative to their CME solar source. The ESP event longitude distribution also showed organization with CME speed. The near-Sun CME speeds (V_i) for these events ranged from ~560 to 2650 km s^{-1} while the average CME transit speeds to 1 au were significantly slower. The angular width of the events had a clear threshold at V_i of ~1300 km s^{-1}, above which events showed significantly larger angular extension compared to events with speeds below. High-speed events also showed larger heavy ion peak intensities near the nose of the shock compared to the flanks while their spectral index was smaller near the nose and larger near the flanks. This organization for events with $V_i < 1300$ km s^{-1} was not as clear. These ESP events were observed over a narrower range of longitudes though the heavy ion peak intensities still appeared largest near the nose of the shock. Their heavy ion spectra showed no clear organization with longitude. These observations highlight the impact of spacecraft position relative to the CME source longitude and V_i on the properties of ESP events at 1 au.

Unified Astronomy Thesaurus concepts: Solar energetic particles (1491); Interplanetary physics (827); Solar coronal mass ejections (310)

1. Introduction

Energetic storm particle (ESP) events are enhancements of energetic particles (ions and electrons) observed during the passage of an interplanetary (IP) shock near 1 au (Bryant et al. 1962). IP shocks are driven by two types of transient flows in the solar wind: (1) transient disturbances known as interplanetary coronal mass ejections (ICMEs; Gosling 1996), and (2) corotating interaction regions (CIRs; Gosling & Pizzo 1999), associated with the interaction of low- and high-speed solar wind streams in IP space. In this study, we focus on ICME-driven ESP events.

The properties of ions and electrons associated with solar energetic particle (SEP) and ESP events observed at 1 au have been widely studied. Cane et al. (1988), for instance, showed that intensity–time profiles of solar proton events depended on the longitude of the observing spacecraft (SC) relative to the solar event and that pronounced proton intensity changes are associated with the arrival of an ICME-driven IP shock. Some ESP events have particle intensity–time profiles with a well-defined change at the shock, like a spike or a step. The duration of this change can vary from several minutes to several hours and days. However, most common ESP profiles are irregular with multiple impulsive intensity variations or show no intensity increases at all (Tsurutani & Lin 1985; Lario et al. 2003; Huttunen-Heikinmaa & Valtonen 2009; Dresing et al. 2016).

The observed ESP properties (e.g., peak intensity, spectral index) tend to depend on several factors such as the SC position along the IP shock, the ICME-driven IP shock properties (e.g., compression ratio, shock normal angle), and the preevent upstream conditions (e.g., seed population, ambient solar wind, and previous events; Desai & Giacalone 2016). Physical parameters thought to impact ESP production include the density compression ratio (van Nes et al. 1984), the upstream seed particle population (Desai et al. 2003; Dayeh et al. 2009), and IP turbulence (Giacalone & Neugebauer 2008). ESP intensities can vary up to at least 5 orders of magnitude between different events; with the strongest correlation being with the CME and/or IP shock speed (Mäkelä et al. 2011; Reames 2012). However, even for events with the same shock or CME speed, ESP events can have widely different intensities. This suggests that the physical processes responsible for producing these enhancements are complex and may depend on more than one parameter.

Multi-SC proton and electron observations of the same ESP event have confirmed differences in the intensity–time profile due to changes of the shock parameters at longitudinally separated locations (Reinhard & Wibberenz 1974; Neugebauer & Giacalone 2005). Ebert et al. (2016) studied oxygen (O) and iron (Fe) properties from seven multi-SC ESP events observed at widely separated 1 au SCs. They found significant variations in both the IP shock and ESP properties between the different SCs observing the same event; however, the correlations between these properties were weak or absent. Their analysis

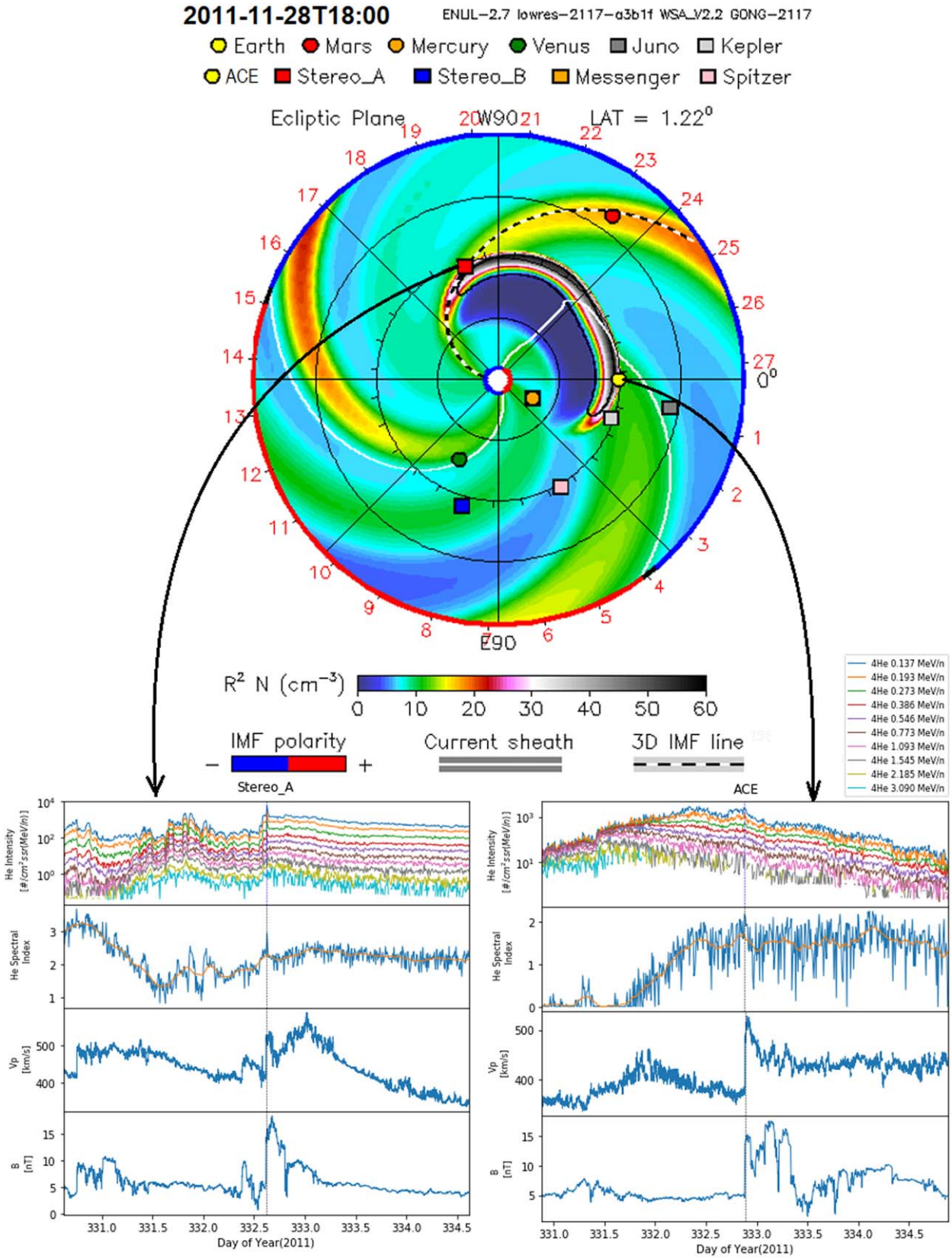

Figure 1. An example of a multi-SC ESP event observed at 1 au. (Top) WSA-ENLIL density simulation of the interplanetary medium during an ICME event observed at both STA (red square) and ACE (yellow circle) on 2011 November 27–29. The simulation was obtained from DONKI. (Bottom) Helium (He) time intensity profiles, He spectral index from ∼0.1–3 MeV/nucleon, solar wind speed, and magnetic field strength observed at STA (Left) and ACE (Right) during the same event. The vertical lines denote the shock arrival time. The orange line in the spectral index panel is the running average of a 21-sample window. This study focuses on both single and multi-SC observations of ESP events at 1 au.

also hinted at an ordering of IP shock (e.g., Mach number) and ESP properties (e.g., peak intensities, spectral index) with respect to the solar source longitude of the CME. For example, the peak O and Fe intensities appeared to be largest at longitudes near the source longitude (a proxy for the nose of the shock) and smaller away from this longitude (a proxy for the shock flank), at least qualitatively. A similar trend has been observed in SEP events at 1 au, where the peak intensities and event fluences are largest at longitudes well connected to the flare and decrease away from those longitudes (Lario et al. 2013; Cohen et al. 2014).

In this study, we examine this spatial ordering of ESP heavy ion (He, O, Fe,) intensities and spectra with longitude in more detail using an expanded list to investigate how they vary along the shock front and with CME speed. As in Ebert et al. (2016), we use the relative longitude from the CME solar source as a proxy for the location of the SC along the CME-driven IP shock. CME speeds near the Sun are obtained from estimates reported in the Space Weather Database of Notifications, Knowledge, and Information (DONKI[6]) while the average CME speeds to 1 au are estimated from the transit time of the event. We focus on both single and multi-SC observations. Section 2 presents the observations used in this study and the method used to select the ESP events. Section 3 presents the results, which are discussed in Section 4. A conclusion and summary are provided in Section 5.

2. Observations

We use data from instruments on board NASA's Advanced Composition Explorer (ACE; Stone et al. 1998) and Solar Terrestrial Relations Observatory (STEREO; Kaiser et al. 2008) missions. ACE is located at the SunEarth L1 Lagrange Point, roughly 0.01 au upstream of Earth. STEREO consists of two SCs, one of them orbiting ahead of Earth (STEREO-A) and the other behind it (STEREO-B), each drifting apart from Earth in opposite directions at about 22° per year. In this configuration, the three SCs provide valuable, different perspectives for studying ESP events at 1 au.

The Suprathermal Ion Telescope (SIT; Mason et al. 2008) on STEREO-A (STA) and STEREO-B (STB), and the Ultra-Low Energy Isotope Spectrometer (ULEIS; Mason et al. 1998) on ACE are used to survey ~0.1–3 MeV/nucleon energetic helium (He), O, and Fe ion observations during all single and multi-SC ESP events identified at these SCs between 2010 January 1 and 2019 December 31. The intercalibration of these instruments is described in several multi-SC studies (Müller-Mellin et al. 2008; Dresing et al. 2009; Cohen & Mewaldt 2018). We used the solar wind plasma and magnetic field instruments on STA and STB (PLASTIC; Galvin et al. 2008 and MAG; Acuña et al. 2008) and ACE (SWEPAM; McComas et al. 1998 and MAG; Smith et al. 1998) to identify the associated IP shocks and their properties and the solar wind conditions upstream and downstream of these structures.

The separation in heliolongitude between ACE, STA, and STB provides an opportunity to study the variability in ESP properties for events observed at different locations (e.g., Figure 1). The top of Figure 1 shows a Wang–Sheely–Arge (WSA)-ENLIL simulation of a CME event on 2011 November 28 obtained from DONKI (Mays et al. 2015). This simulation shows the density configuration in the inner heliosphere on day of year (DOY) 332, 2011 at 18:00 UT. The arc-like structure traveling through the inner heliosphere is the ICME-driven shock front observed between ~E30 and W120 with respect to Earth (yellow dot) heliolongitude and showing densities from ~10 to ~60 $R^2N(cm^{-3})$. The simulation suggests that STA and ACE were in the path of this ICME-driven shock, STA at the western flank and ACE at the eastern flank. The time profiles of energetic He intensities, He spectral index (see Section 3.5 for details on how the spectral index is computed), solar wind speed, and magnetic field strength are shown at the bottom of Figure 1. The CME-driven shock shown in Figure 1 was observed at STA on DOY 332, 2011, at 14:51 UT, and ~6.4 hr later at ACE on DOY 332, 2011 at 21:14 UT.

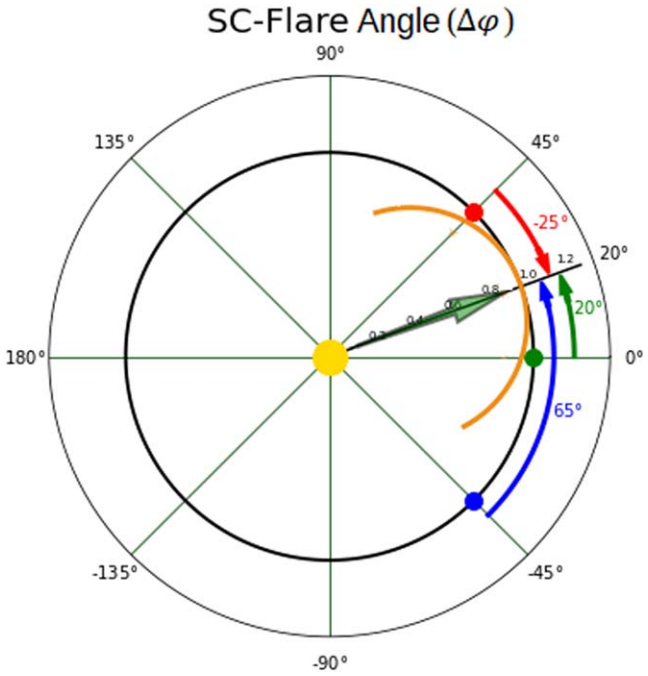

Figure 2. A demonstration for how the spacecraft (SC)-flare angle shown in Table 1 is calculated. The SC-flare angle ($\Delta\phi$) is the difference between the longitude of the solar flare, used to approximate the CME solar source, and the longitude of the SC that observes the ESP event at 1 au. This angle is used as a proxy for the location of the SC along the IP shock (orange arc) with 0° being at the nose of the shock. In this example, the flare longitude is at 20° with respect to Earth. ACE (green) is at 0°, STA (red) is at 45°, and STB (blue) is at −45°. Therefore the SC-flare angles are 20°−0° = 20° for ACE, 20°–45° = −25° for STA, and 20°–(−45°) = 65° for STB.

2.1. ESP Event Selection

To select an event, we use information provided by DONKI and other CME lists.[7,8,9,10,11] The CME parameters in the DONKI list were determined using the NASA CCMC's Stereoscopic CME Analysis Tool (StereoCAT) based on triangulation of transient CME features from multiple coronagraph fields of view (Pulkkinen et al. 2009; Mays et al. 2015), and NOAA Space Weather Prediction Center's CME Analysis Tool (CAT) based on tracking the volumetric structure of CMEs (Pizzo & Biesecker 2004; Millward et al. 2013). There are

[6] https://kauai.ccmc.gsfc.nasa.gov/DONKI/

[7] https://cor1.gsfc.nasa.gov/catalog/

[8] https://stereo-ssc.nascom.nasa.gov/pub/ins_data/impact/level3/

[9] http://www.srl.caltech.edu/ACE/ASC/DATA/level3/index.html

[10] http://www.ssg.sr.unh.edu/mag/ace/ACElists/obs_list.html

[11] https://cdaw.gsfc.nasa.gov/CME_list

Table 1
List of ESP Events Used in This Study, Including the Shock Arrival Time, Observing Spacecraft (SC), Source Flare Location and the Near-Sun and Average Transit CME Speeds

Event Number (1)	Year (2)	Shock Arrival DOY/Time (3)	SC (4)	SC Longitude (deg) (5)	Flare Longitude (deg) (6)	Flare Latitude (deg) (7)	SC-Flare Angle($\Delta\phi$) (deg) (8)	CME Speed at 21.5 R_{Sun} (km s^{-1}) (9)	Average CME Transit Speed (km s^{-1}) (10)
Multi-SC Events									
1	2011	68/06:47	STA	87.3	50	17	−37.3	1980	1154
	2011	69/06:10	ACE	0.0	50	17	50.0	1980	717
2	2011	332/14:51	STA	105.6	45	23	−60.6	930	717
	2011	332/21:14	ACE	0.0	45	23	45.0	930	670
3	2012	29/13:04	STA	107.0	75	40	−32.0	2200	940
	2012	30/15:37	ACE	0.0	75	40	75.0	2200	603
4	2012	75/12:35	ACE	0.0	43	25	43.0	2250	973
	2012	75/22:31	STA	109.6	43	25	−66.6	2250	758
5	2012	247/07:11	STB	−124.9	−63	−15	61.9	1498	716
	2012	247/11:23	ACE	0.0	−63	−15	−63.0	1498	662
6	2013	66/12:23	STB	−139.7	−135	10	4.7	1900	750
	2013	67/02:20	STA	131.0	−135	10	94.0	1900	570
7	2014	58/16:8	ACE	0.0	−78	−11	−78.0	1670	663
	2014	59/04:22	STB	−160.4	−78	−11	82.4	1670	560
Single-SC Events									
8	2010	215/16:55	ACE	0.0	−34	24	−34.0	1362	734
9	2010	254/06:55	STA	82.0	96	8	14.0	850	719
10	2010	348/17:12	STA	84.3	50	−10	−34.3	750	663
11	2011	17/15:44	STB	−90.8	−125	16	−34.2	680	409
12	2011	49/00:38	ACE	0.0	15	−20	15.0	920	592
13	2011	57/08:24	STB	−94.0	−100	−18	−6.0	900	867
14	2011	78/11:24	STA	88.0	75	17	−13.0	690	632
15	2011	87/08:53	STB	−95.0	−125	7	−30.0	1005	831
16	2011	90/23:38	STB	−95.0	−115	6	−20.0	1320	822
17	2011	155/19:57	ACE	0.0	−30	−5	−30.0	950	689
18	2011	168/02:01	ACE	0.0	−45	5	−45.0	830	631
19	2011	251/16:00	STA	103.4	74	36	−29.4	606	464
20	2011	254/08:51	STA	103.5	130	35	26.5	1040	691
21	2011	269/11:52	ACE	0.0	−45	12	−45.0	1507	890
22	2011	276/22:22	STB	−97.7	−120	0	−22.3	1500	857
23	2011	280/11:24	STB	−98.1	−155	35	−56.9	1370	598
24	2011	298/04:51	STA	105.0	90	52	−15.0	990	609
25	2011	316/05:18	ACE	0.0	−35	24	−35.0	1150	653
26	2011	324/13:38	STB	−103.8	−118	27	−14.2	773	645
27	2011	330/18:09	STA	105.5	61	40	−44.5	718	435
28	2011	360/23:50	STB	−109.3	−128	−17	−18.7	572	458
29	2012	4/16:40	STA	106.2	99	−17	−7.2	1152	806
30	2012	24/14:30	ACE	0.0	26	41	26.0	2211	1204
31	2012	57/20:55	ACE	0.0	−12	32	−12.0	815	638
32	2012	63/9:56	STA	108.8	140	11	31.2	558	550
33	2012	68/10:45	ACE	0.0	−23	4	−23.0	1800	1247
34	2012	68/13:37	STB	−117.5	−60	30	57.5	2200	1134
35	2012	72/8:42	ACE	0.0	5	22	5.0	1400	1078
36	2012	86/16:29	STB	−118.4	−161	11	−42.6	1600	658
37	2012	88/21:37	STB	−118.4	−105	15	13.4	1450	904
38	2012	108/3:36	STB	−118.7	−110	15	8.7	1000	848
39	2012	114/2:27	ACE	0.0	−18	−28	−18.0	650	502
40	2012	139/12:42	STA	115.0	75	−15	−40.0	1500	1143
41	2012	196/17:26	ACE	0.0	−6	−17	−6.0	1400	856
42	2012	267/14:28	STA	122.2	150	12	27.8	1040	709
43	2012	273/18:37	STA	122.6	170	−20	47.4	1592	710
44	2012	282/4:30	ACE	0.0	10	−28	10.0	650	568
45	2012	316/21:19	STA	125.1	132	−10	6.9	752	547
46	2012	317/22:15	ACE	0.0	−11	−13	−11.0	570	527
47	2012	331/7:57	STA	125.9	138	30	12.1	975	706

Table 1
(Continued)

Event Number (1)	Year (2)	Shock Arrival DOY/Time (3)	SC (4)	SC Longitude (deg) (5)	Flare Longitude (deg) (6)	Flare Latitude (deg) (7)	SC-Flare Angle($\Delta\phi$) (deg) (8)	CME Speed at 21.5 R_{Sun} (km s^{-1}) (9)	Average CME Transit Speed (km s^{-1}) (10)
48	2013	59/21:14	STA	130.5	125	10	−5.5	900	675
49	2013	76/5:27	ACE	0.0	−2	−3	−2.0	1485	893
50	2013	103/22:12	ACE	0.0	−25	−7	−20.0	675	664
51	2013	112/10:08	STA	134.7	110	2	−24.7	800	779
52	2013	117/23:32	STA	135.2	170	−4	34.8	880	642
53	2013	124/4:52	STB	−142.7	−120	12	22.7	860	570
54	2013	139/22:20	ACE	0.0	−40	13	−40.0	1400	682
55	2013	178/16:17	STA	140.7	172	−11	31.3	732	473
56	2013	186/7:04	STB	−145.0	−85	11	60.0	915	519
57	2013	206/6:12	STA	142.0	170	20	28.0	700	678
58	2013	234/07:05	STA	143.4	180	17	36.6	1200	714
59	2013	252/14:32	STB	−147.5	−125	15	22.5	750	638
60	2013	275/1:20	ACE	0.0	38	26	38.0	1100	820
61	2013	281/4:54	STB	−148.5	−139	−26	9.5	1000	602
62	2013	281/19:40	ACE	0.0	6	−15	6.0	790	784
63	2013	308/8:56	STA	147.0	145	5	−2.0	1078	765
64	2013	362/17:06	STB	−151.4	−134	−31	17.4	1600	683
65	2014	7/14:26	ACE	0.0	4	−35	4.0	695	639
66	2014	9/19:31	ACE	0.0	30	−24	30.0	2061	846
67	2014	36/3:27	STA	151.3	140	−20	−11.3	745	606
68	2014	47/7:50	STA	151.9	127	−6	−24.9	1080	848
69	2014	52/7:17	STB	−159.5	−151	−13	8.5	810	835
70	2014	73/23:09	STB	−162.1	−154	30	8.1	1150	743
71	2014	84/19:25	ACE	0.0	−35	4	−35.0	700	657
72	2014	102/2:27	STB	−164.3	−158	0	6.3	690	564
73	2014	110/10:22	ACE	0.0	10	−34	10.0	1400	919
74	2014	223/9:03	STA	163.6	177	−18	13.4	780	627
75	2014	246/7:45	STB	−168.3	−155	15	13.3	1700	946
76	2014	247/6:00	STB	−168.3	−109	−8	48.3	1400	755
77	2014	255/15:26	ACE	0.0	10	15	10.0	1400	921
78	2014	314/1:37	ACE	0.0	−26	21	−26.0	800	749
79	2015	173/17:59	ACE	0.0	−8	7	−8.0	1500	1061
80	2015	175/12:57	ACE	0.0	3	14	3.0	1155	981
81	2015	263/5:27	ACE	0.0	7	−26	7.0	1030	858
82	2015	297/18:26	ACE	0.0	37	−13	37.0	861	657
83	2015	365/0:02	ACE	0.0	14	−15	14.0	850	700
84	2017	197/5:16	ACE	0.0	40	−9	40.0	1200	804
85	2017	255/19:32	ACE	0.0	85	−12	85.0	2650	809
86	2017	262/2:55	STA	−127.8	−163	−3	−35.2	1404	1029
87	2018	46/7:50	ACE	0.0	22	−7	22.0	734	530

Note. The angles are in Heliocentric Earth Equatorial (HEEQ) coordinates. The SC-flare angle is used as a proxy for the location of the observing SC with respect the nose of the CME shock.

matrices to convert the plane-of-sky velocities to the same coordinate system (Heliocentric Earth Equatorial (HEEQ) coordinates in this case for CME simulation). Please see Section 3 of Mays et al. (2015) and Section 2 of Wold et al. (2018) for details. We identify the most probable location of the CME solar source, approximated by the location of the associated solar flare, the CME speed at 21.5 solar radii (R_{Sun}), and the shock time at the observing SC for each event using existing CME and flare lists and estimates from the DONKI. We compare the longitude of the CME solar source to that of the observing SC at 1 au and use the difference ($\Delta\phi$) as a proxy for the location of the observing SC along the IP shock when it arrives at 1 au (similar to Lario et al. 2016).

Figure 2 shows an example of this calculation. In our survey, we initially identified 10 multi-SC and 151 single-SC candidate ESP events. By visually inspecting the plots, we selected the events where the energetic particle intensity profiles show a synchronized increase of at least 200% within ±3 hr of the shock arrival time in the He, O, and Fe intensities at each energy bin (10 bins for He as seen in Figure 1, 9 bins for O and 11 bins for Fe) between 0.1–3 MeV/nucleon, and no other dominant shocks were present within a 1 day window. Thus, we selected 7 multi-SC and 80 single-SC events, which showed clear ESP intensities enhancements, most of which peak at or near the shock. Table 1 lists the events used in this study.

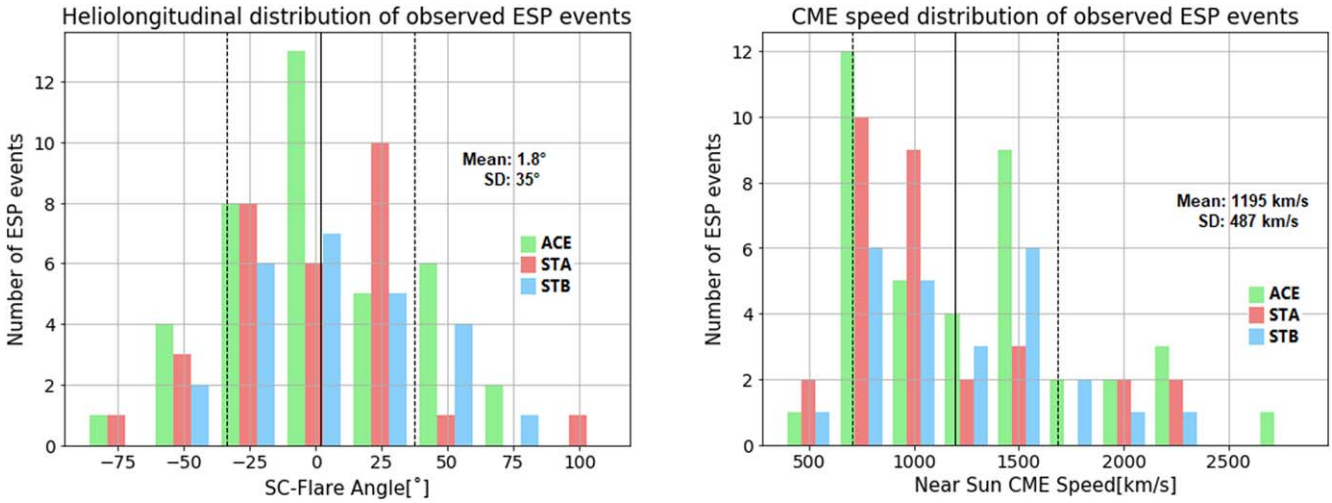

Figure 3. (Left) Longitudinal distribution of ESP events observed at ACE (green), STEREO-A (red), and STEREO-B (blue) relative to the solar source of their associated CME, approximated by the flare location for each event. The mean and standard deviation for this distribution are plotted with a black solid and dashed line, respectively. (Right) Distribution of near-Sun CME speeds at 21.5 solar radii ($R_{\rm Sun}$) for ESP events observed at ACE (green), STA (red), and STB (blue). The mean and standard deviation are plotted with a black solid and dashed line, respectively.

The first seven events in Table 1 are multi-SC events observed at two SCs separated in heliolongitude; there are no ESP events observed by three or more SCs in our study. Column 1 shows the event number. Columns 2 and 3 show the year, the day of year (DOY) and shock arrival time at the observing SC. Column 4 identifies the observing SC. Column 5 shows the SC longitude. Columns 6 and 7 show the longitude and latitude, respectively, of the associated flare. Column 8 shows the difference between the flare longitude and that of the observing SC (see Figure 2). Column 9 shows the estimated CME speed at 21.5 solar radii (V_i) as indicated in DONKI, which is the speed at the leading edge of the CME, not scaled toward the flanks. Column 10 shows the average CME transit speed from the Sun to the observing SC near 1 au.

3. Results

3.1. ESP Heliolongitude Distribution at 1 au

The histogram at the left of Figure 3 shows the distribution of ESP heavy ion (He, O, Fe) events observed by STA, STB, and ACE (red, blue, and green, respectively) as a function of the SC-flare angle defined above (see Figure 2). The location of the CME solar source is approximated by the solar flare location for each event (Ontiveros & Vourlidas 2009). The events are grouped into bins of 25°. The mean value for all the events is 1.8°, with a standard deviation of 35°. Events near 0° are interpreted as being near the nose of the shock while events at large angles are interpreted as being near the shock flanks.

3.2. CME Speed Distribution for ESP Events

The histogram at the right of Figure 3 shows the distribution of near-Sun CME speed (V_i) for the ESP events listed in Table 1, grouped into speed bins of 250 km s^{-1}. The speeds are based on estimates at 21.5 solar radii ($R_{\rm Sun}$) as reported in DONKI. The events had near-Sun CME speeds ranging from 558 to 2650 km s^{-1}, with a median and mean speed of 1040 and 1195 km s^{-1}, respectively. The near-Sun CME speeds are used to examine their impact on ESP properties observed at 1 au. To quantify the average CME transit speed between the Sun and 1 au, we compute the average CME transit speed of each event using

$$\bar{V}_T = R/(t_{1\rm au} - t_{R_{Sun}}), \quad (1)$$

where R is the Sun–SC distance, $t_{1\rm au}$ is the shock arrival time at the observing SC (about 1 au), and $t_{R\rm Sun}$ is the CME onset time observed on the Sun reported by DONKI. A similar approach was used by Lario et al. (2016) in a multi-SC event where the observers were located at different heliolongitudes and radial distances from the Sun.

Figure 4 shows the histogram of the average CME transit speed for each ESP event studied here. The CMEs have a mean transit speed of 738 km s^{-1} with a standard deviation of 176 km s^{-1} and a median of 707 km s^{-1}. This distribution is more symmetric than the distribution shown at the right of Figure 3 for the near-Sun CME speeds and the transit speeds are significantly lower.

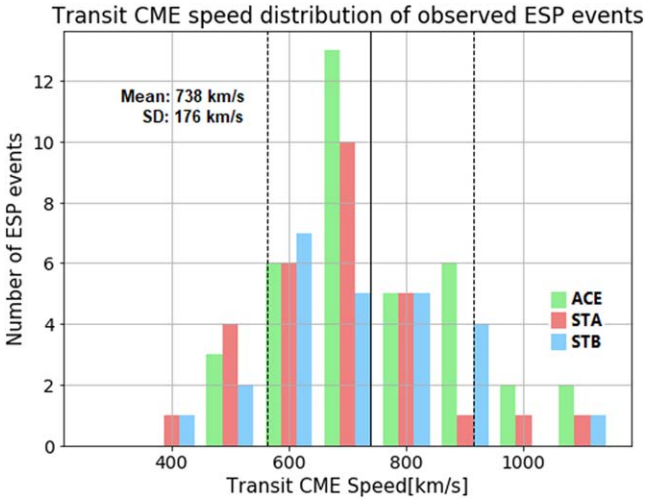

Figure 4. Histogram of average CME transit speeds at 1 au for ESP events observed at the ACE (green), STA (red), and STB (blue) SC, grouped into bins of 100 km s^{-1}.

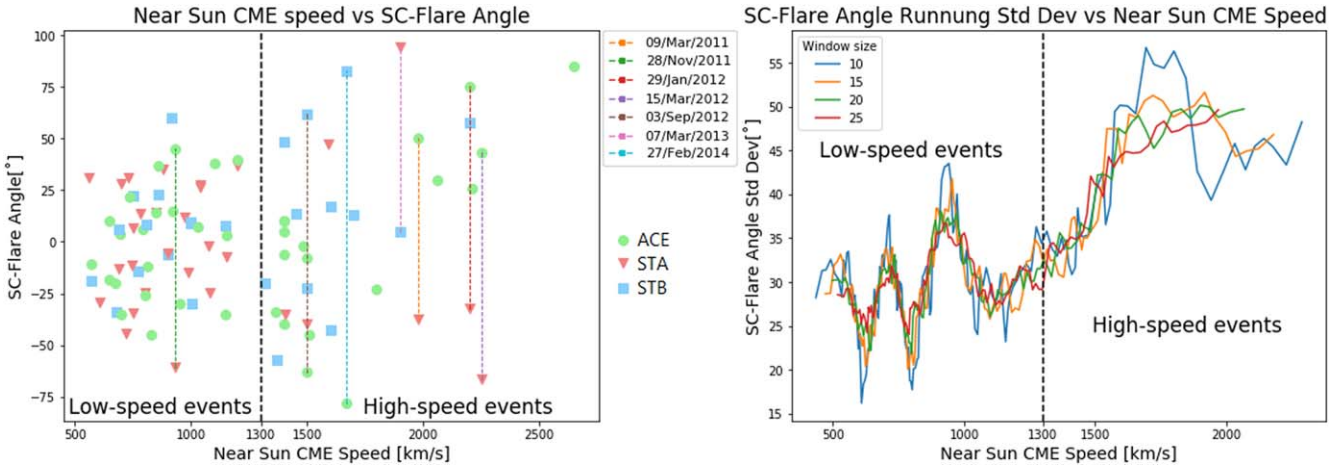

Figure 5. (Left) Near-Sun CME speed at 21.5 solar radii vs. the SC-flare angle for ESP events observed at 1 au. STEREO-A, STEREO-B, and ACE observations are shown with red triangles, blue squares, and green circles, respectively. Multi-SC events are connected by colored dashed lines. (Right) Running average of the standard deviation for the SC-flare angle as a function of near-Sun CME speed. Running average windows of 10, 15, 20, and 25 events are used in the analysis.

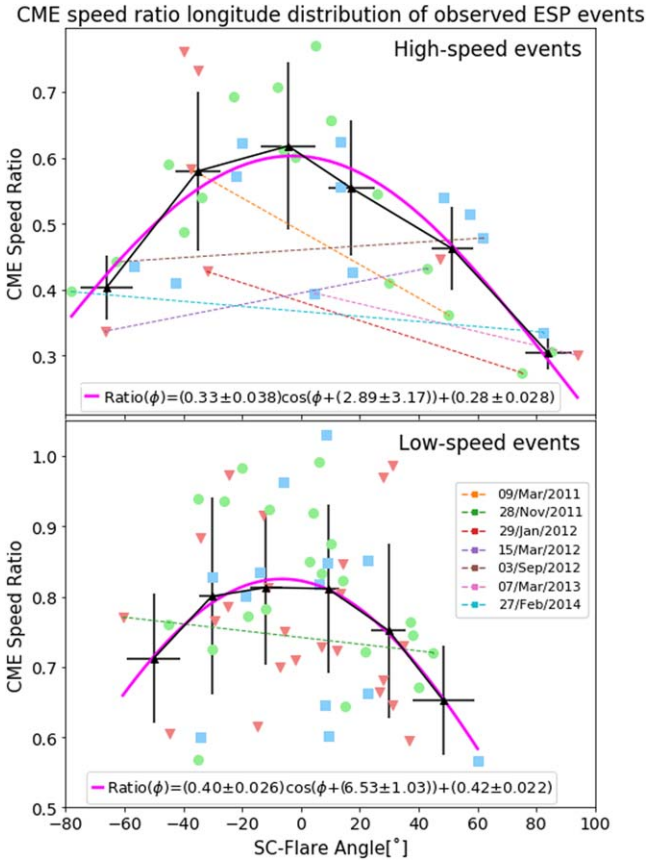

Figure 6. Longitudinal distribution of the ratio between the transit time and near-Sun CME speeds for the high-speed (top plot) and low-speed (bottom plot) ESP events listed in Table 1. The events were divided into six bins of which the mean and standard errors are shown with black crosses. The purple fit is described in the text. Symbols have the same format as in Figure 5.

3.3. ESP Heliolongitude versus Near-Sun CME Speed

The left of Figure 5 shows a scatterplot of near-Sun CME speed versus the SC-flare angle described in Figure 2 for the ESP events in Table 1. The ESP events ranged from $-78°$ to $+94°$ in SC-flare angle, and from 558 to 2650 km s^{-1} in near-Sun CME speed. We see that the ESP event longitude distribution is wider at higher CME speeds and there are fewer events at the highest speeds. The right of Figure 5 plots the running average standard deviation for the SC-flare angle as a function of near-Sun CME speed. The running average shows that the standard deviation has a threshold at $\sim$1300 km s^{-1}, a speed where the width of the ESP events shows a significant increase (right of Figure 5). This threshold is used to divide the events by high and low speed.

A majority (86%) of the multi-SC ESP events are associated with CMEs having near-Sun speeds $>$1300 km s^{-1}. The impact of CME longitude and speed on ESP heavy ion properties at 1 au is investigated below.

Figure 6 shows the relation between the near-Sun CME speed and the average CME transit speed shown in Figures 3 and 4, respectively, as a function of longitude for high (top) and low (bottom) speed events (defined in Figure 5). This relation is expressed by the following ratio:

$$CME\ Speed\ Ratio = \bar{V}_T / V_i. \quad (2)$$

The longitude is the difference in heliolongitude between the observing SC and CME solar source as defined in Figure 2. For each group, this plot compares the CME speed at 21.5 $R_{\rm Sun}$ and 1 au at different longitudes for the ESP events in Table 1. In the high-speed group, for example, at 0°, the CME speed at 1 au is, on average, $\sim$60% of the estimated value at 21.5 $R_{\rm Sun}$; whereas at $-70°$ it is $\sim$40% of its near-Sun value. The events in each plot are divided into six bins and the mean and standard deviation of each bin, shown as gray triangles and crosses, respectively, were plotted. An expression for the CME speed ratio as a function of longitude,

$$\text{CME Speed Ratio}(\Delta\phi) = V_0 \cos(\Delta\phi - \phi_0) + V_1, \quad (3)$$

was fit to the bin mean values, where V_0 is the cosine amplitude (0.33 ± 0.038 and 0.40 ± 0.026 for high- and low-speed events, respectively), $\Delta\phi$ is the longitude between the observer and the CME solar source, ϕ_0 is the offset longitude of the shock front nose ($2\overset{\circ}{.}89 \pm 3\overset{\circ}{.}17$ and $6\overset{\circ}{.}53 \pm 1\overset{\circ}{.}03$ for high- and low-speed events, respectively), and V_1 is an offset fitting constant (0.28 ± 0.028 and 0.42 ± 0.022 for high- and low-speed events, respectively). The angle ϕ_0 is more significant for low-speed events than for high-speed events compared with their respective errors. This expression is used below to define

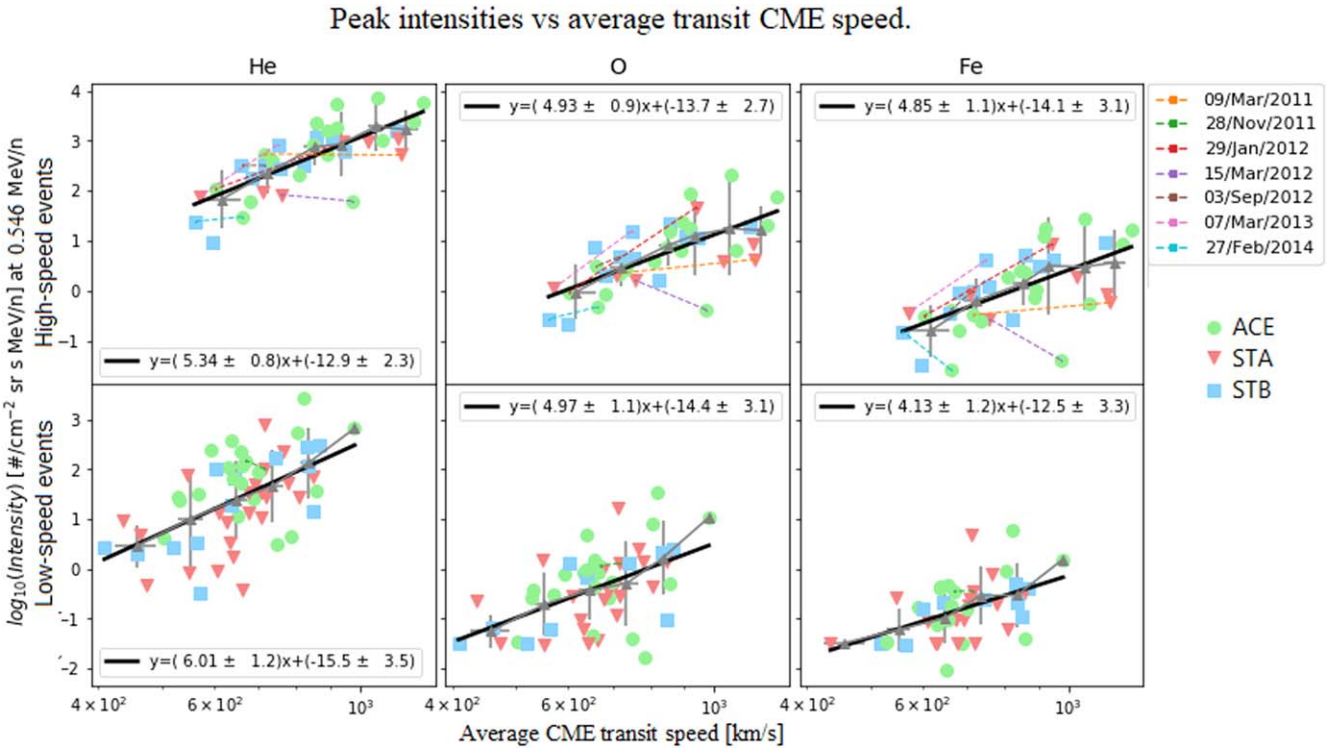

Figure 7. Peak intensities at 0.546 MeV/n for He, O, and Fe ions vs. the average CME transit speed. The black line denotes the fit to the data and the equation for the fit is shown in each plot, where $x = \log_{10}$ (average transit CME speed) and $y = \log_{10}$(Intensity). Symbols have the same format as in Figure 5.

the average CME transit speed as a function of near-Sun CME speed and longitude. Notice that one CME speed ratio is greater than 1, in the low-speed group, which could result from plane-of-sky projection effects or an error in the near-Sun CME speed estimate for the event. Lario et al. (2016) found a similar trend in a multi-SC event where they used the expression $V(\Delta\phi) = V_0\cos(\Delta\phi) + V_1$ proposed by Smart & Shea (1985). We normalized the equation by the near-Sun CME speed, and added an angular offset (ϕ_0) to the expression, which allows the shock nose to be displaced from 0°.

3.4. ESP Heavy Ion Peak Intensities versus CME Speed and Source Longitude

We use a 1 hr window bounding the shock times (30 minutes before and after the shock) to identify the peak He, O, and Fe intensities at each energy bin (10 bins for He as seen in Figure 1, 9 bins for O and 11 bins for Fe) between 0.1–3 MeV/nucleon, for the ESP events identified in Table 1.

Figure 7 shows the peak intensities at 0.546 MeV/n for He, O, and Fe versus the average transit CME speed. Here, He is more abundant than O by about 2 orders of magnitude and O is more abundant than Fe by about 1 order of magnitude at this energy. We see that the peak heavy ion intensities increase with increasing CME speed, which is similar to the results of Kahler (2001), Gopalswamy et al. (2004), and Reames (2013) for protons and helium. These observations are fitted by this expression:

$$\log_{10}(j) = C_1 \log_{10}(\bar{V}_T) - C_0, \quad (4)$$

where C_1 is the slope and C_0 is the y-intercept of the log − log fit that correlates the average CME transit speed and ESP peak intensities for each species at this energy. Notice how the slope ($C1$) is steeper for lighter species, which suggests that lighter ion peak intensities have a stronger dependence on the CME transit speed than heavier species. In turn, the CME transit speed depends on the near-Sun CME speed and the SC-flare longitude according to the following relation derived in Figure 6:

$$\bar{V}_T = V_i(V_0\cos(\Delta\phi - \phi_0) + V_1). \quad (5)$$

Inserting Equation (5) into Equation (4), we obtain a relation for the ESP peak intensities as a function of the near-Sun CME speed (V_i) and longitude ($\Delta\phi$):

$$\log_{10}(j) = C_1 \log_{10}(V_i(V_0\cos(\Delta\phi - \phi_0) + V_1)) - C_0. \quad (6)$$

Figure 8 shows the distribution of ESP He, O, and Fe peak intensities at 0.546 MeV/n with respect to the SC-flare angle for the events in Table 1. The events in the top panels have near-Sun CME speeds greater than 1300 km s^{-1} while the events in the bottom panels have speeds less than that value. The high-speed ESP events show a clear organization with the SC-flare longitude. In this group, the ESP events located close to 0° (approximated as the nose of the CME-driven shock at 1 au) have peak intensities up to 2–3 orders of magnitude higher than those events at large longitudes, approximated as the flanks of the shock. On average, these events also tend to have larger peak intensities than events with lower near-Sun CME speeds. Equation (6) is overplotted (purple curve) to the bin mean values and shows good agreement with the observations. The lower-speed ESP events in the bottom panels are confined to a narrower range of longitudes and do not show as clear a trend, though the peak intensities do in general appear to be largest

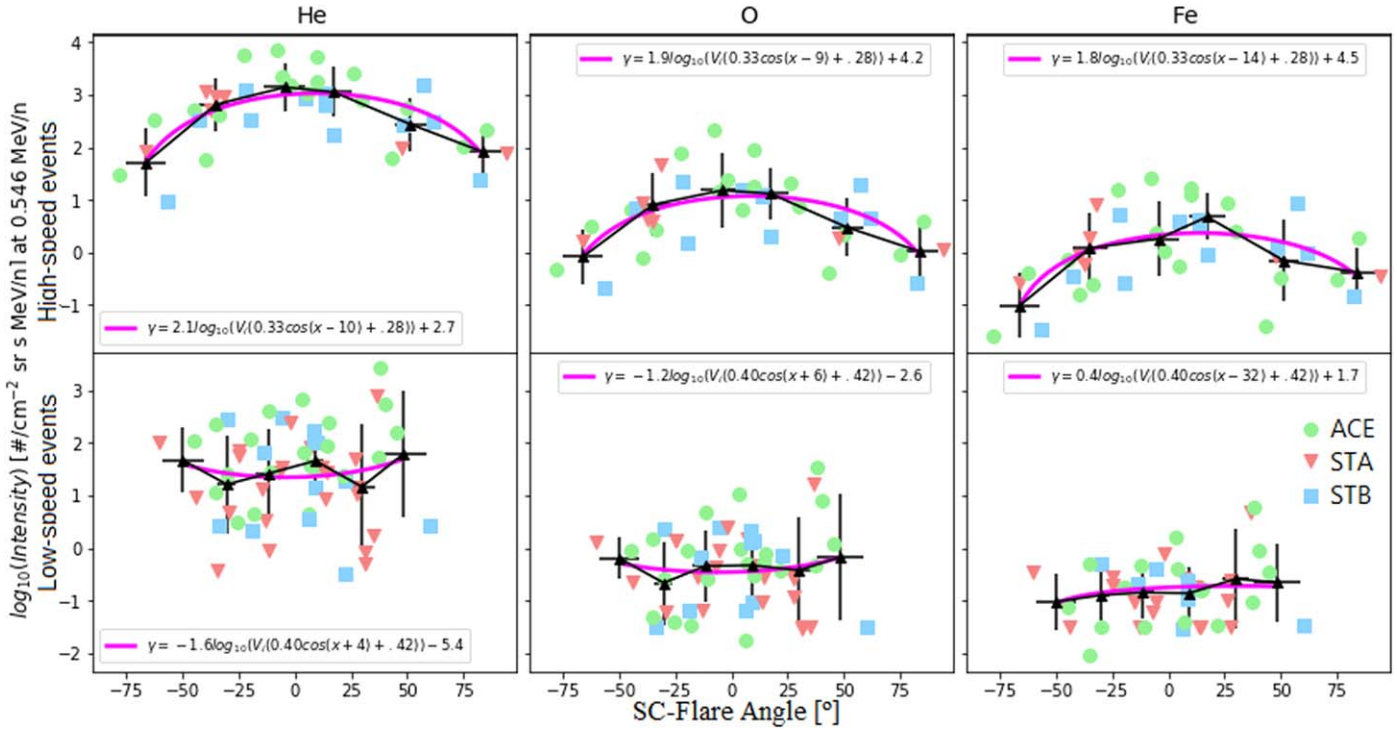

Figure 8. ESP Peak intensity of He, O, and Fe at 0.546 MeV/nucleon vs. the SC-flare angle. Events with high near-Sun CME speeds are shown in the top panels while events with lower near-Sun CME speeds are shown in the bottom panels. In each plot, the events were divided into six bins. The black symbols and crosses denote the mean and standard deviation for each bin, respectively. The purple line is the fit to the bin mean values based on Equation (6), where the median near-Sun CME speed was used as V_i. Symbols have the same format as in Figure 5.

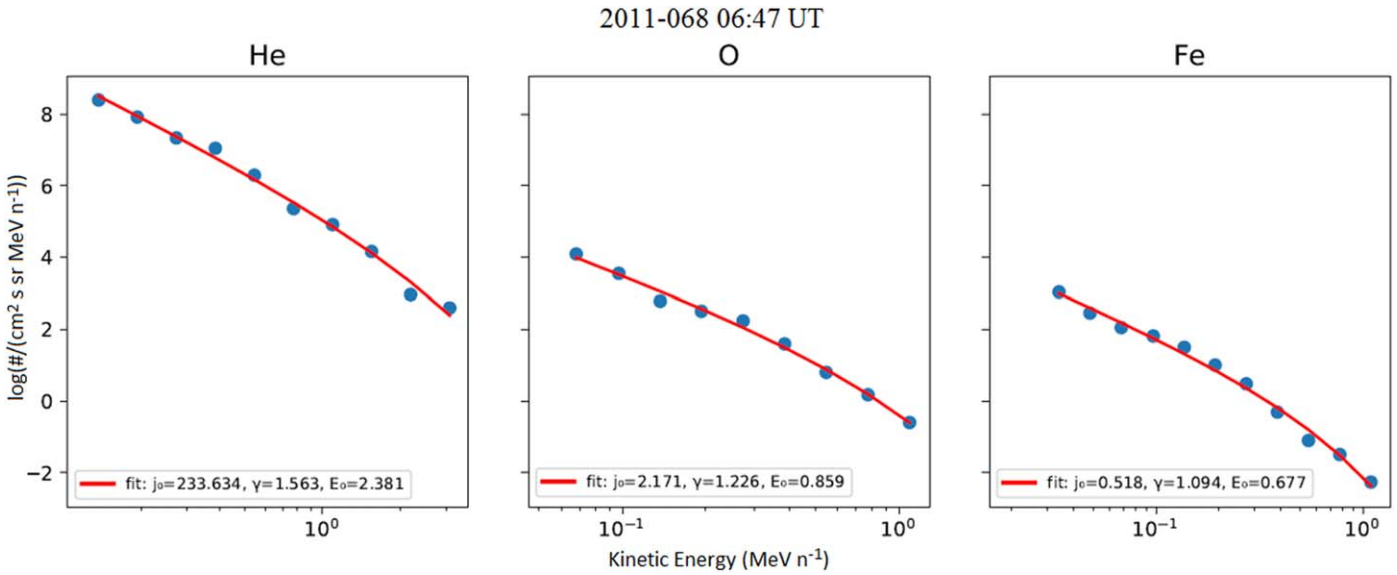

Figure 9. Energy spectra of He, O, and Fe as observed by STEREO-A/SIT at the shock arrival time of the ESP event on 2011 March 9. The solid curves show fits with the Jones & Ellison (1991) expression (see the text for details).

near 0°. We observe similar trends for 0.1–1 MeV/n ions (not shown).

3.5. ESP Heavy Ion Spectra

We next examine the dependence of the He, O, and Fe spectral index on CME source longitude and near-Sun CME speed. We fit the ~0.1–3.0 MeV/nucleon He, O, and Fe spectral profile of the ESP events of Table 1 with the Jones & Ellison (1991) expression of $j(E) = j_0 E^{(-\gamma)}\, e_{(-E/E_0)}$, where j is the differential intensity, E is the particle energy in MeV/nucleon, γ is the spectral index, and E_0 is the e-folding energy. The highest intensity value of each energy range bin, within a ±30 minute window about the shock time, was taken for this calculation. Figure 9 shows an example of the fits and their parameters using the described technique.

To study the ESP spectra as a function of CME speed and location along the shock, we follow a similar approach as applied to the peak intensities. We obtain an expression relating the ESP spectral index, γ, to the average CME transit speed,

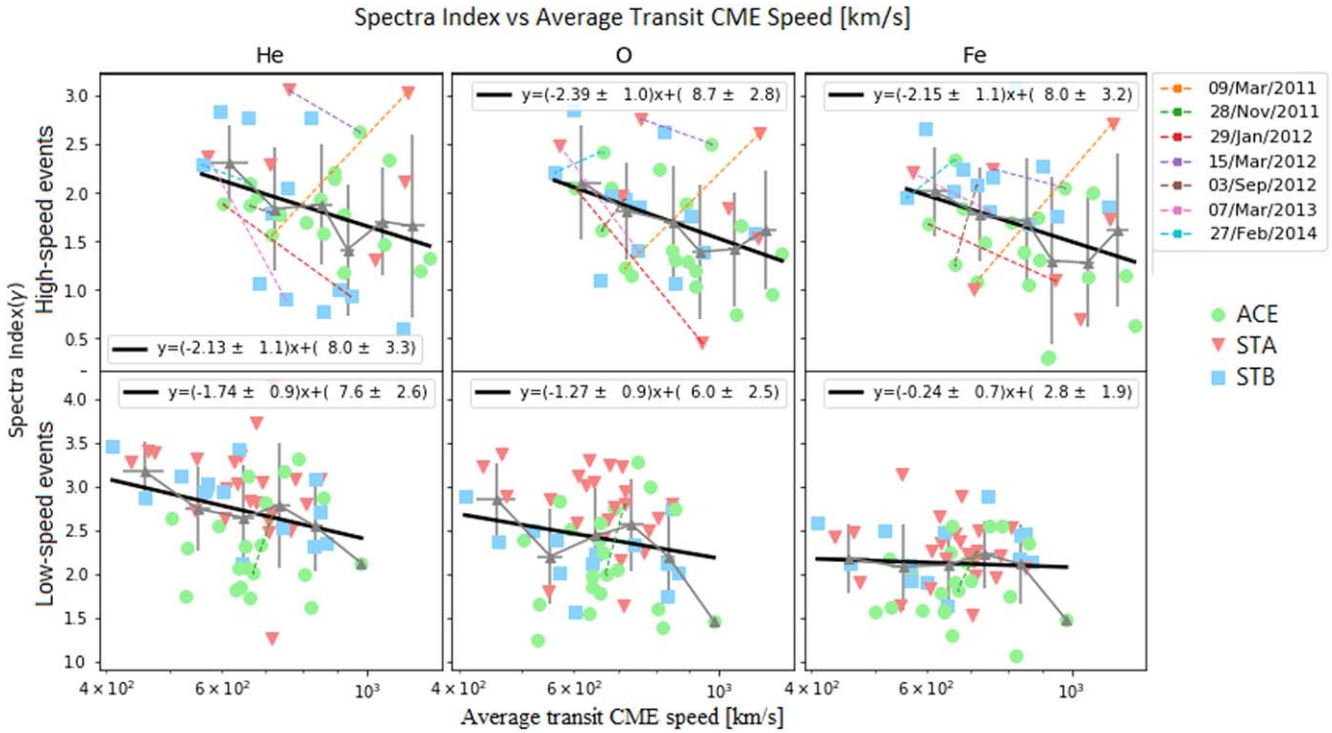

Figure 10. Spectral index of 0.1–3 MeV/n He, O, and Fe ions vs. the average CME transit speed. The ESP events observed by STA, STB, and ACE SCs are shown in red, blue, and green, respectively. The multi-SC events are linked with a straight, dashed line. The black line denotes the fit to the data where x is the log10(average CME transit speed) and y is the spectral index, γ. Symbols have the same format as in Figure 5.

which is then combined with Equation (5) to obtain an expression relating γ to the near-Sun CME speed and SC-flare longitude.

Figure 10 shows the 0.1–3 MeV/n He, O, and Fe spectral index with respect to the average CME transit speed. For the high-speed events, the spectral index shows a general decrease with increasing CME transit speed, though the observations show significant scatter. The spectral index for the high-speed events is generally smaller (with means of 2.25 for He, 2.04 for O, and 2.05 for Fe) than for those associated with the low-speed events (with means of 3.03 for He, 2.80 for O, and 2.42 for Fe). The fit to the data has the form

$$\gamma = C_1 \log_{10}(\bar{V}_T) - C_0, \quad (7)$$

where γ is the spectral index, $\bar{V}_T$ is the average transit CME speed, C_1 is the slope and C_0 the y-intercept of the fitting line. The events were divided into five bins and the mean and standard deviation of each bin are shown with gray triangles and crosses, respectively. The fit generally follows the trend denoted by the gray symbols.

Inserting Equation (5) into Equation (7), we obtain a relation for the ESP spectra as a function of the near-Sun CME speed (V_i) and longitude ($\Delta\phi$):

$$\gamma = C_1 \log_{10}(V_i(V_0 \cos(\Delta\phi - \phi_0) + V_1)) - C_0, \quad (8)$$

Figure 11 shows the longitudinal distribution of the spectral index for 0.1–3 MeV/nucleon He, O, and Fe ions for the events of Table 1. The plots in the top panels are for events with near-Sun speeds greater than 1300 km s^{-1}. The spectral index in these events are, in general, smaller (harder) near the nose of the shock and larger (softer) near the flanks. This suggests more efficient acceleration near the nose of the shock in the events associated with higher near-Sun CME speeds. The function defined in Equation (8) shows good agreement with the mean value bins for these observations.

The heavy ion spectral index for ESP events with low near-Sun CME speeds shown in the bottom panels display no apparent ordering with longitude. In general, the heavy ion spectra for ESP events with high CME speeds have a smaller (harder) spectral index than events with low CME speeds.

No trends were found for the distribution of E_0 given that this parameter was not resolvable over the used energy range for about 50% of the events.

4. Discussion

We surveyed energetic heavy ion, plasma, and magnetic field observations during 80 single-SC and 7 multi-SC ESP events identified at the STEREO-A, STEREO-B, and ACE SCs between 2010 January 1 and 2019 December 31. We examined the impact of CME source longitude and near-Sun CME and average CME transit speeds on variations in the 0.1–3 MeV/n He, O, and Fe peak intensities, and spectral index for these events.

The longitudinal distribution of heavy ion ESP events observed at 1 au peaked when the SC-flare angle between the observing SC and the CME source on the Sun was small, the distribution of events having a mean value of 1.8° and with a standard deviation of 35°. This suggests that ESPs are likely more efficiently accelerated near the nose of the associated IP shock compared to the flanks. This is especially clear for heavy ion ESPs driven by low-speed CMEs, which are observed primarily at longitudes of $<\pm 50°$ (see Figure 5—left plot). Similar results are reported by Mäkelä et al. (2011) for proton and electron ESPs.

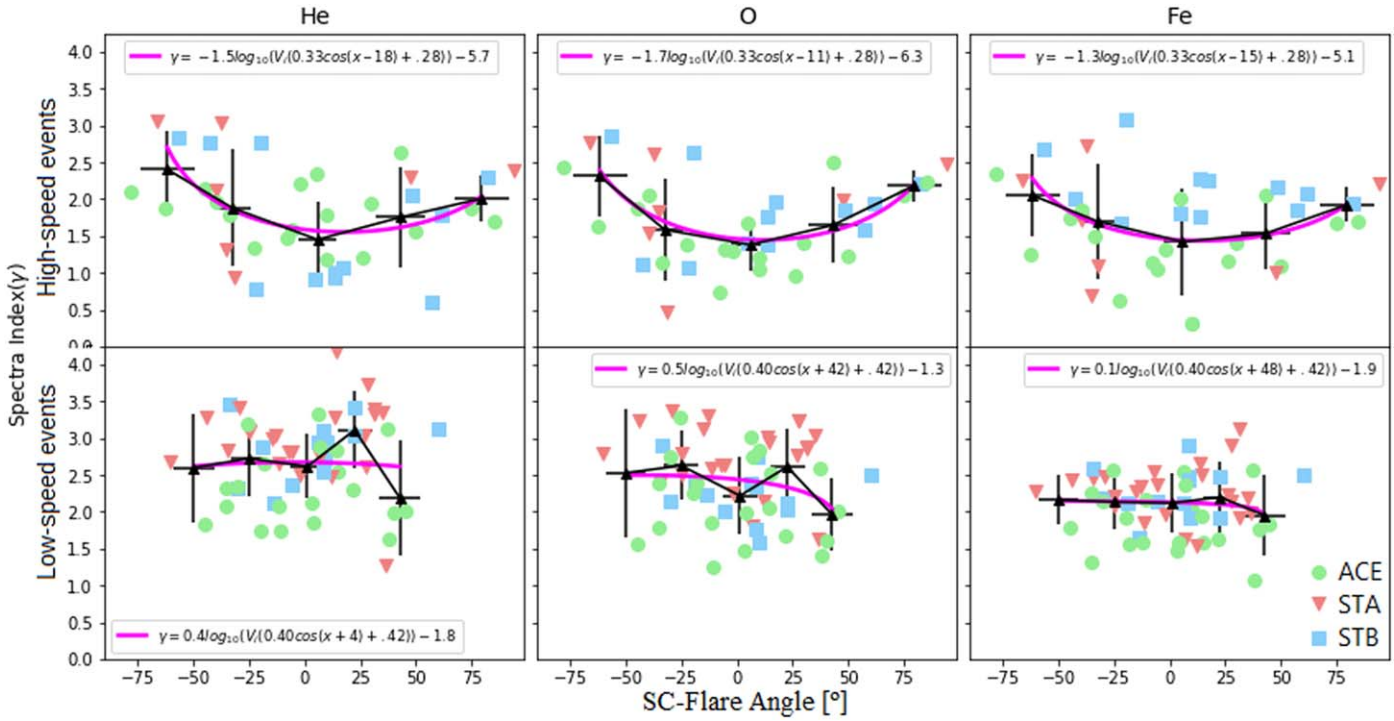

Figure 11. Longitudinal distribution of spectral index for 0.1–3 MeV/nucleon He, O, and Fe ions for the events in Table 1. The events were divided into five bins of which the mean and standard errors are shown with black triangles and crosses, respectively. The purple line is the fit to the bin means using the function defined by Equation (8), where the median near-Sun CME speed of the events was used as V_i. Symbols have the same format as in Figure 5.

The distribution of near-Sun CME speeds associated with the ESP events studied here was not symmetric and had several fast events with speeds extending to $>1500\,\mathrm{km\,s^{-1}}$. ESPs that had large SC-flare angles were typically associated with high-speed CMEs. There was a clear change in the angular distribution of these events at near-Sun speeds of $\sim 1300\,\mathrm{km\,s^{-1}}$, the standard deviation of the angular distribution ranging from $\sim 20°$ to 40° for speeds below this value and $\sim 30°$–55° for speeds above this value (Figure 5). This implies that high near-Sun CME speeds are required to produce wide-angle ESP events (e.g., with measurable intensity enhancements along IP-shock flank). This is consistent with the results from Gopalswamy et al. (2014) that wide-angle CMEs are associated with faster CMEs.

The average transit CME speeds at 1 au was also calculated for these events (see Equation (1)) following an approach outlined in Lario et al. (2016) for a multi-SC SEP event study. The distribution of average transit speeds was more symmetric than that of the near-Sun CME speeds. The transit speeds were significantly lower than the near-Sun CME speeds. The average CME transit speed distribution for eastern events (SC-flare angle <0) had a mean value of $740\,\mathrm{km\,s^{-1}}$, a median of $686\,\mathrm{km\,s^{-1}}$, and a standard deviation of $190\,\mathrm{km\,s^{-1}}$; whereas, for western events (SC-flare angle >0) had a mean value of $732\,\mathrm{km\,s^{-1}}$, a median of $709\,\mathrm{km\,s^{-1}}$, and a standard deviation of $164\,\mathrm{km\,s^{-1}}$. While we do not expect the CME transit speed to show an east–west asymmetry, the eastern events in our survey had slightly faster CME transit speeds (by about 1%) than western events.

The ESP events were separated into low- and high-speed events based on the trends observed in the ESP angular distribution versus near-Sun CME speed. The ESP heavy ion peak intensities showed a strong correlation with CME transit speed, increasing with increasing speed, for both low- and high-speed events. These results are consistent with those from previous studies (e.g., Mäkelä et al. 2011 for ions and electrons; Reames 2012 for He). The high-speed events also showed a clear organization between the peak intensity and SC-flare longitude, suggesting a longitudinal ordering of the peak intensities along the CME-driven IP shock, with higher intensities near the nose of the shock and lower intensities along the flanks. Similar trends have been observed in SEP events at 1 au, where the peak intensities and event fluences are largest at longitudes well connected to the flare and decrease away from those longitudes (Lario et al. 2013; Cohen et al. 2014; Lario et al. 2016). For low-speed ESP events, the longitudinal distribution is less organized most likely due to the absence of events seen at SC-flare longitudes $>\pm 50°$.

To characterize the trend in peak intensity with longitude, we derived a phenomenological formula for the peak He, O, and Fe intensities as a function of near-Sun CME speed and SC-flare longitude. This was done by combining the equations for peak intensity as a function of CME transit speed in Figure 7 with the expression for the CME speed in Equation (5). The resulting expression (Equation (6)) captures the average trend of the observations and can be used as a forecasting tool for peak heavy ion intensities at 1 au based on remote observations of the near-Sun CME speed and flare longitude.

The ESP heavy ion spectral index also showed a dependence with SC-flare longitude for the high-speed events. The spectral indices, on average, were smaller (harder) near the nose of the shock and larger (softer) near the flanks. This result was shown qualitatively by Ebert et al. (2016) in a study of seven multi-SC heavy ion(O and Fe) ESP events. In this study, using more events than Ebert et al. (2016; 87 versus 7), we found that for He, O, and Fe, the ESP events associated with high-speed CMEs have a harder energy spectra when observed at small

SC-flare angles (Figure 11), indicating that the shocks associated with these events are more efficient in accelerating particles at the nose compared to the flanks of the shock front. However, the ESP events driven by low-speed CMEs did not show a clear trend in the spectral index versus SC-flare longitude. This is possibly because low-speed CMEs likely drive weaker shocks than high-speed CMEs and the characteristic spectral indices expected from the steady state diffusive shock acceleration (DSA) theory is $3s/(s-1)$ where s is the density compression ratio of the shock. Therefore, the indices are softer for shocks associated with low-speed CMEs than those associated with high-speed CMEs. However, if the shock characteristic spectrum is softer than the spectrum of the seed particles, DSA yields an accelerated particle spectrum with the spectral index given by the seed population (see e.g., Li 2017). Consequently, the accelerated particle spectral index at strong shocks is less affected by the seed population spectral index than at weak shocks.

Overall, the results of this study show that heavy ion ESP events associated with CMEs having near-Sun speeds $>\sim$1300 km s^{-1} display a longitudinal ordering in their peak intensities and spectral indices. The results support the claims that particle acceleration is more efficient near the nose of an IP shock compared to the flanks, especially in events with high near-Sun CME speeds.

5. Summary and Conclusions

The key results of this study are as follows:

1. The probability of observing an ESP event at 1 au is highest when the observing SC is at longitudes near the CME solar source.
2. The near-Sun CME speeds for these events ranged from $\sim$560 to 2650 km s^{-1}, with mean and median speeds of 1195 km s^{-1} and 1040 km s^{-1}, respectively.
3. The average CME transit speeds at 1 au were significantly slower than the near-Sun speeds, with a mean and median of 738 km s^{-1} and 706 km s^{-1}, respectively. This distribution was symmetric about the mean.
4. The longitude distribution of ESP events is organized by near-Sun CME speed, the angular width of the events showing a threshold at $\sim$1300 km s^{-1}. Events above this threshold show significantly larger angular extent compared to events with speeds below this threshold.
5. The heavy ion peak intensities and spectral indices for events with fast ($>$1300 km s^{-1}) near-Sun CME speeds show a clear organization along the CME shock at 1 au. The peak intensities are largest and spectral indices are smallest, near 0° longitude, which we interpret as the nose of the shock. The peak intensities show up to a 2–3 order of magnitude decrease along the shock flanks while the spectral indices are up by a factor of 2–3 larger, i.e., softer at flanks.
6. The longitudinal dependence for events with slow ($<$1300 km s^{-1}) near-Sun CME speeds is less clear. The ESP events are observed over a narrower range of longitudes and the heavy ion peak intensities and spectral index do not show a clear organization with longitude.

In conclusion, we find that ESP heavy ion peak intensities and spectral indices show clear organization with the CME source longitude and CME speed. Shocks associated with fast CMEs near the Sun produce ESPs over broader longitudes compared to those associated with lower-speed CMEs. The fast events show clear evidence of more efficient acceleration at the nose of the shock for $\sim$0.1–3 MeV/nucleon heavy ions compared to the shock flank, as evident by the higher peak intensities and smaller (harder) spectral indices.

Work at SwRI and UAH was supported by NASA grants NNX17AI17G and 80NSSC19K0079. L.K.J. was supported by NASA's LWS and HSR programs and Science Mission Directorate as part of the STEREO project. M.A.D. acknowledges partial support from NASA grant 80NSSC20K0290. We gratefully thank the STEREO/SIT, PLASTIC, and MAG and ACE/ULEIS, SWEPAM, and MAG teams for the use of their data and making their data publicly available. We thank NASA's Community Coordinated Modeling Center for making the WSA-ENLIL simulations publicly available through the Space Weather Database of Notifications, Knowledge, Information (DONKI).

ORCID iDs

A. Santa Fe Dueñas https://orcid.org/0000-0002-6035-1254
R. W. Ebert https://orcid.org/0000-0002-2504-4320
M. A. Dayeh https://orcid.org/0000-0001-9323-1200
M. I. Desai https://orcid.org/0000-0002-7318-6008
L. K. Jian https://orcid.org/0000-0002-6849-5527
G. Li https://orcid.org/0000-0003-4695-8866
C. W. Smith https://orcid.org/0000-0002-5379-1542

References

Acuña, M. H., Curtis, D., Scheifele, J. L., et al. 2008, SSRv, 136, 203
Bryant, D. A., Cline, T. L., Desai, U. D., & McDonald, F. B. 1962, JGR, 67, 4983
Cane, H. V., Reames, D. V., & von Rosenvinge, T. T. 1988, JGRA, 93, 9555
Cohen, C. M. S., Mason, G. M., Mewaldt, R. A., & Wiedenbeck, M. E. 2014, ApJ, 793, 35
Cohen, C. M. S., & Mewaldt, R. A. 2018, SpWea, 16, 1616
Dayeh, M. A., Desai, M. I., Dwyer, J. R., et al. 2009, ApJ, 693, 1588
Desai, M., & Giacalone, J. 2016, LRSP, 13, 3
Desai, M. I., Mason, G. M., Dwyer, J. R., et al. 2003, ApJ, 588, 1149
Dresing, N., Gómez-Herrero, R., Heber, B., et al. 2009, SoPh, 256, 409
Dresing, N., Theesen, S., Klassen, A., & Heber, B. 2016, A&A, 588, A17
Ebert, R. W., Dayeh, M. A., Desai, M. I., et al. 2016, ApJ, 831, 153
Galvin, A. B., Kistler, L. M., Popecki, M. A., et al. 2008, SSRv, 136, 437
Giacalone, J., & Neugebauer, M. 2008, ApJ, 673, 629
Gopalswamy, N., Akiyama, S., Yashiro, S., et al. 2014, GeoRL, 41, 2673
Gopalswamy, N., Yashiro, S., Krucker, S., Stenborg, G., & Howard, R. A. 2004, JGRA, 109, A12105
Gosling, J. T. 1996, ARA&A, 34, 35
Gosling, J. T., & Pizzo, V. J. 1999, SSRv, 89, 21
Huttunen-Heikinmaa, K., & Valtonen, E. 2009, AnGeo, 27, 767
Jones, F. C., & Ellison, D. C. 1991, SSRv, 58, 259
Kahler, S. W. 2001, JGRA, 106, 20947
Kaiser, M. L., Kucera, T. A., Davila, J. M., et al. 2008, SSRv, 136, 5
Lario, D., Aran, A., Gómez-Herrero, R., et al. 2013, ApJ, 767, 41
Lario, D., Ho, G. C., Decker, R. B., et al. 2003, in AIP Conf. Proc. 679, SOLAR WIND TEN: Proc. of the Tenth Int. Solar Wind Conf. (Melville, NY: AIP), 640
Lario, D., Kwon, R.-Y., Vourlidas, A., et al. 2016, ApJ, 819, 72
Li, G. 2017, ScChD, 60, 1440
Mäkelä, P., Gopalswamy, N., Akiyama, S., Xie, H., & Yashiro, S. 2011, JGRA, 116, A08101
Mason, G. M., Gold, R. E., Krimigis, S. M., et al. 1998, SSRv, 86, 409
Mason, G. M., Korth, A., Walpole, P. H., et al. 2008, SSRv, 136, 257
Mays, M., Taktakishvili, A., Pulkkinen, A., et al. 2015, SoPh, 290, 1775
McComas, D. J., Bame, S. J., Barker, P., et al. 1998, SSRv, 86, 563
Millward, G., Biesecker, D., Pizzo, V., & de Koning, C. A. 2013, SpWea, 11, 57

Müller-Mellin, R., Böttcher, S., Falenski, J., et al. 2008, in The Solar Electron and Proton Telescope for the STEREO Mission, ed. C. T. Russell (New York: Springer), 363
Neugebauer, M., & Giacalone, J. 2005, JGRA, 110, A12106
Ontiveros, V., & Vourlidas, A. 2009, ApJ, 693, 267
Pizzo, V. J., & Biesecker, D. A. 2004, GeoRL, 31, L21802
Pulkkinen, A., Oates, T., & Taktakishvili, A. 2009, SoPh, 261, 115
Reames, D. V. 2012, ApJ, 757, 93
Reames, D. V. 2013, SSRv, 175, 53
Reinhard, R., & Wibberenz, G. 1974, SoPh, 36, 473
Smart, D. F., & Shea, M. A. 1985, JGRA, 90, 183
Smith, C. W., L'Heureux, J., Ness, N. F., et al. 1998, SSRv, 86, 613
Stone, E. C., Frandsen, A. M., Mewaldt, R. A., et al. 1998, SSRv, 86, 1
Tsurutani, B. T., & Lin, R. P. 1985, JGRA, 90, 1
van Nes, P., Reinhard, R., Sanderson, T. R., Wenzel, K.-P., & Zwickl, R. D. 1984, JGRA, 89, 2122
Wold, A. M., Mays, M. L., Taktakishvili, A., et al. 2018, JSWSC, 8, A17